Activity-induced asymmetric dispersion in confined channels with constriction

Armin Maleki [1], Malihe Ghodrat [1,*] and Ignacio Pagonabarraga [2,3,†]
[1] *Department of Physics, Faculty of Basic Sciences, Tarbiat Modares University, P.O. Box 14115-175, Tehran, Iran*
[2] *Departament de Física de la Matèria Condensada, Universitat de Barcelona, Carrer de Martí i Franqués 1, 08028 Barcelona, Spain*
[3] *Universitat de Barcelona Institute of Complex Systems (UBICS), Universitat de Barcelona, 08028 Barcelona, Spain*

(Received 17 May 2023; accepted 16 November 2023; published 18 January 2024)

Microorganisms, such as *Escherichia coli*, are known to display upstream behavior and respond rheotactically to shear flows. In particular, *E. coli* suspensions have been shown to display strong sensitivity to spatial constrictions, leading to an anomalous densification past the constriction for incoming fluid velocities comparable to the microoganism's self-propulsion speed. We introduce a Brownian dynamics model for ellipsoidal self-propelling particles in a confined channel subject to a constriction. The model allows us to identify the relevant parameters that characterize the relevant dynamical regimes of the accumulation of the active particles at the constriction, and clarify the mechanisms underlying the experimental observations. We find that particles are trapped in butterfly-like attractors in front of the constriction, which is the origin of the symmetry breaking in the emerging density profiles of active particles passing the constriction. In addition, the probability of trapping and thus the strength of asymmetry are affected by size of the particles and geometry of the channel, as well as the ratio of fluid velocity to propulsion speed.

DOI: 10.1103/PhysRevFluids.9.013103

I. INTRODUCTION

Microorganisms can be found in a wide variety of media and complex environments [1]. Their emergent, collective behavior is a result of the interrelated motion due to the incoming flow features and the disturbance microorganisms generate. Such hydrodynamic coupling significantly alters the rheological properties of active suspensions [2], modifies how microorganisms swim and disperse, and strongly impacts the regimes of solute transport [3]. This leads to a wide and rich variety of emerging behavior, which includes anomalous viscosity [4], mixing enhancement, bioconvection, or anomalous dispersion [5]. In the presence of a shear flow, they show rheotactic behavior [6], which depends on the microorganism shape and mode of locomotion [7]; e.g., for flagellates, the interaction of the moving flagella with the shear flow is known to play a critical role. Positive rheotaxis, i.e., upstream navigation, has been observed under confinement for a variety of microorganisms, such as sperm cells in the reproductive tract [8], bacteria in the upper urinary tract, and *Escherichia coli* in catheters [9].

In particular, when microorganisms swim close to confining walls, their behavior can be qualitatively altered, leading to chiral trajectories and upstream motion [10]. Microorganisms in such

*m.ghodrat@modares.ac.ir
†ipagonabarraga@ub.edu

conditions show a high sensitivity to morphological variabilities of the confining substrate [11]. Such coupling and sensitivity has strong implications for the behavior of microorganisms in porous media, how they are transported or dispersed, and how they organize and accumulate inside such heterogeneous media [12,13].

The collective behavior of microswimmers in confined channels and in the presence of constrictions has significant implications for the transport and dispersion of bacteria in fluid environments [14]. These tiny organisms have constitutive properties that differ significantly from passive suspensions, leading to new and surprising effects such as activated Brownian motion, anomalous viscosity, mixing enhancement, bioconvection, and work extraction from fluctuations.

Despite the practical implications for biocontamination in porous rocks, biological microvessels, and medical catheters, the fundamental question of hydrodynamic dispersion of bacteria suspended in a fluid remains a challenge [15]. Current methods of analysis rely on macroscopic convection-diffusion equations with adsorption-desorption terms to describe retention effects by surfaces [16]. However, systematic inconsistencies between experiment and modeling suggest the need for further refinements, including the detailed interaction of individual microorganisms and the confining substrate. Studies of simplified geometries and model pores provide systematic analysis and understanding of the response of microorganisms under confinement. For example, recent experiments [17] have quantified the dispersion of *E. coli* through a funnel, showing an anomalous downstream densification of the microorganisms for incoming fluid velocities comparable to the self-propulsion speed of *E. coli*.

In this work we will introduce a simple, general theoretical model that describes the motion of self-propelling particles (SPPs) in a channel characterized by a constriction, subject to an incoming fluid flow. The model allows us to identify the relevant dimensionless parameters that characterize how SPPs accumulate around the constriction and helps to identify the physical mechanisms that control the motion and organization of SPPs around a constriction. In Sec. II we introduce the model and details of the geometry and the methodology to solve it. Section III identifies the relevant dimensionless parameters that identify the relevant dynamical regimes of SPPs suspensions. Subsequently, Sec. IV systematically presents the relevant quantities that characterize the emerging behavior of SPPs in a confined channel in the presence of a constriction. The paper finishes by highlighting the main results obtained and their implications in Sec. V.

II. MODEL AND SIMULATION TECHNIQUES

The model system consists of N SPPs swimming in a rectangular channel of length L_x and height L_y, with a constriction described by a Gaussian

$$f(x) = h \exp\left(-\frac{(x - x_{\text{mid}})^2}{2\sigma^2}\right), \tag{1}$$

with height $h = 80$ μm, expanded over a length $\sigma = 50$ μm (for the lower boundary), as shown in Fig. 1(a). In the centering point ($x_{\text{mid}} = 0$), the channel reaches the minimum width of $L_c = L_y - 2h$, which varies between 15–240 μm in our simulations. The suspending media in the channel is a Newtonian fluid of density $\rho = 1000\,\text{kg}\,\text{m}^{-3}$ and dynamic viscosity $\eta = 0.88$ mPa s at temperature $T = 298$ K. The size of SPPs is typically 1–10 μm and their self-propulsion velocity $v_s \sim O(10)\ \mu\text{m}\,\text{s}^{-1}$.

This velocity induces low Reynolds number flows for spherical particles of radius a [18],

$$\text{Re}_s = \frac{\rho v_s a}{\eta} \sim 10^{-5},$$

in which the inertial forces are negligible compared to the viscous forces that swimming objects experience in the fluid [19]. In the following we present the details of our assumptions for suspending fluid, swimming particles, and boundaries.

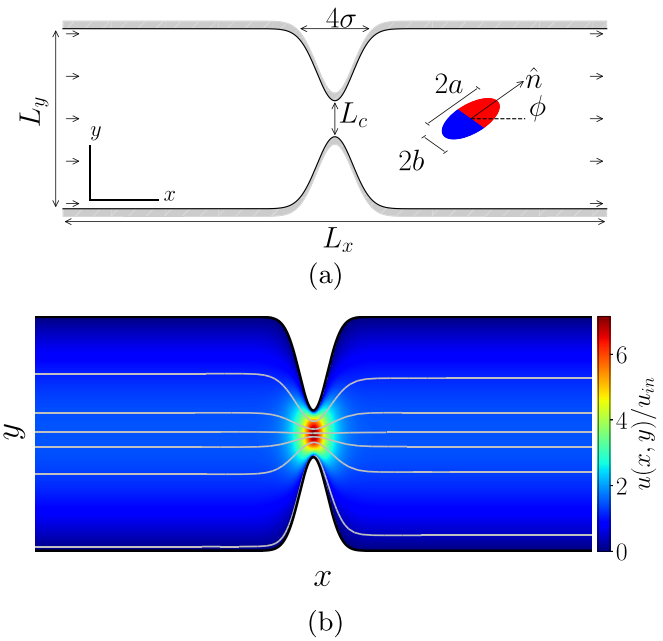

FIG. 1. (a) Schematic of the system used in this study, displaying the relevant geometry and parameters. (b) Velocity field and streamlines in the channel of $L_x = 4$ mm, $L_y = 200$ μm, $L_c = 40$ μm, incoming velocity $u_{\text{in}} = 5$ μm s^{-1} and average velocity in the constriction $\langle u_x \rangle_c = 24.35$ μm s^{-1}.

A. Fluid

The suspending fluid enters the left side of the channel with incoming velocity u_{in} due to a pressure gradient and forms a laminar flow with typical average velocity $\langle u \rangle \sim O(10)$ μm s^{-1}, such that the flow can also be considered as a laminar one in low Reynolds regime [20],

$$\text{Re}_f = \frac{\rho \langle u \rangle L_x}{\eta} \sim 10^{-2}.$$

The fluid velocity field in the channel, $\mathbf{u}(\mathbf{r})$, is obtained by solving the linear form of Navier-Stokes equation, which reduces to the Stokes equation at vanishingly Reynolds numbers

$$\eta \nabla^2 \mathbf{u} = \nabla P. \tag{2}$$

The fluid is assumed to be an incompressible Newtonian fluid, $\nabla \cdot \mathbf{u} = 0$, and ∇P denotes the pressure gradient [20]. Equation (2) is solved numerically by the finite element method on discrete points in space with a no-slip boundary condition on the channel walls. Figure 1(b) indicates the velocity field $[\mathbf{u}(x, y)]$ and streamlines for a channel with incoming velocity $u_{\text{in}} = 5$ μm s^{-1} and funnel width, $L_c = 40$ μm. The fluid velocity attains its maximum value at the center of the constriction and goes to zero in the vicinity of the walls, as expected. Additionally, due to continuity and incompressibility, the average velocity in the constriction, $\langle u_x \rangle_c$, is linearly proportional to the incoming velocity (or equivalently the fluid velocity far from the constriction) for arbitrary channel widths:

$$\frac{\langle u_x \rangle_c}{u_{\text{in}}} \propto \frac{L_y}{L_c}.$$

B. Particles

The motility of spherical and/or elliptical particles, swimming in the channel, are modeled by two-dimensional overdamped Langevin equations

$$\dot{\mathbf{r}} = v_s\hat{\mathbf{n}} + \mathbf{u}(\mathbf{r}) + \sqrt{2D_T}\,\xi_r \tag{3}$$

$$\dot{\phi} = \Omega_0 + \Omega_f(\mathbf{r}) + \sqrt{2D_R}\,\xi_\phi, \tag{4}$$

in which $\hat{\mathbf{n}} = (\cos\phi, \sin\phi)$ indicates the particle polarity and ϕ denotes the angle in polar coordinates. In this model, which is best known as an active Brownian particle (ABP) model, D_T and D_R represent the translational and rotational diffusion coefficients, respectively. For spherical particles of radius a, the rotational diffusion is $D_R = k_BT/8\pi\eta a^3$ and $D_T = 4a^2D_R/3$. The corresponding expressions for an ellipsoidal particle moving or rotating in parallel ($D_\parallel$) and perpendicular ($D_\perp$) directions to its major axis are given in [21]. We have used the average value of these coefficients as an approximation of the effective translational and rotational diffusion coefficients. Alternatively, empirical values for the special SPP under study can be used.

The noise term ξ, is a zero averaged, $\langle\xi\rangle = 0$, uncorrelated, $\langle\xi_\alpha(t)\xi_\beta(t')\rangle = \delta_{\alpha\beta}\delta(t-t')$, random process described by a Gaussian distribution, which simulates the thermal fluctuations experienced by the particles in their translational (ξ_r) and rotational (ξ_ϕ) motion.

The self-propelling term, $v_0\hat{\mathbf{n}}$, provides a directed motion which couples the translational and rotational degrees of freedom through the polarity vector. The term $\mathbf{u}(\mathbf{r})$ accounts for the background fluid velocity. In the dilute regime, which is the situation to be considered in this work, it can be assumed that the fluid velocity (as well as the fluid viscosity) is not affected in the presence of self-propelling particles. Therefore, the fluid velocity obtained from Eq. (2) is taken as a time-independent quantity in the Langevin equation.

On the other hand, according to Jeffery's equation [22], the spherical and/or ellipsoidal particles experience a torque due to the nonuniform field of the fluid velocity that applies asymmetric forces on the upper and lower parts of the propelling objects. The resulting angular velocity, $\Omega_f(\mathbf{r})$, for 2D ellipsoidal particles reads

$$\Omega_f(\mathbf{r}) = \frac{1}{2}(u_{yx} - u_{xy}) + \frac{\beta}{2}(u_{yx} + u_{xy})\cos(2\phi) - \beta\sin(2\phi), \tag{5}$$

where $\beta = (\lambda^2-1)/(\lambda^2+1)$ defines the shape eccentricity, $\lambda = a/b$, being the ratio of semimajor to semiminor axis of ellipsoids (or aspect ratio). In the special case of spherical particles ($\beta = 0$), the above equation reduces to

$$\Omega_f(\mathbf{r}) = \tfrac{1}{2}(u_{yx} - u_{xy}), \tag{6}$$

with $u_{xy} = \partial u_x/\partial y$, which are numerically discretized as

$$u_{xy} = \frac{u_x(x, y+\delta y) - u_x(x, y)}{\delta y}.$$

The first term in Eq. (4) considers the intrinsic angular velocity, Ω_0, caused by chirality, which is zero for the symmetric spherical or ellipsoidal particles used in this study. We have neglected the interparticle interactions since we consider dilute suspensions. The system is not subject to external forces.

C. Boundaries

The upper and lower boundaries are solid walls which return the colliding particle back to the channel, based on a mirror reflection from the tangential line at the colliding point, which acts only on a particle's position while leaving its angle unchanged [23]. As a result, SPPs will experience successive collisions with the wall, typically on a timescale $\tau = D_R^{-1}$, before a significant change in their propulsion direction detaches them from the wall; see, e.g., the typical trajectories in

Fig. 10 below. We disregard the finite size of the particles when colliding with a wall and apply the reflection rule when the particle's center of mass crosses the wall. This minimal model avoids the computational cost of determining the colliding point of an ellipsoid with the wall. On the side walls, we consider periodic boundary conditions; a particle that exits one side of the channel enters the opposite side while its vertical position and propelling direction are kept unchanged. Hence, we conserve particle number and minimize system size effects.

III. DIMENSIONLESS EQUATIONS

Using the inverse of the rotational diffusion constant $\tau_p = D_R^{-1}$, at timescale $\hat{t} = t/\tau_p$, and the characteristic size of the SPPs a as reference length scale ($\hat{r} = r/a$), we can rewrite Eqs. (3) and (4) in dimensionless form:

$$\dot{\hat{\mathbf{r}}} = \mathrm{Pe}_s \hat{\mathbf{n}} + \mathrm{Pe}_f \hat{\mathbf{u}}(\hat{\mathbf{r}}) + \sqrt{2\hat{D}_T}\, \hat{\xi}_r, \tag{7}$$

$$\dot{\hat{\phi}} = \hat{\Omega}_0 + \hat{\Omega}_f(\mathbf{r}) + \sqrt{2}\, \hat{\xi}_\phi, \tag{8}$$

where we have chosen the incoming fluid velocity, u_{in}, as the characteristic velocity of the fluid flow [24], such that $\hat{\mathbf{u}}(\hat{\mathbf{r}}) = \mathbf{u}(\mathbf{r})/u_{\mathrm{in}}$, $\hat{\Omega}(\hat{\mathbf{r}}) = D_R^{-1}\Omega(\mathbf{r})$, $\hat{\xi} = D_R^{-1/2}\xi$, and the dimensionless parameter

$$\hat{D}_T = \frac{D_T}{a^2 D_R}$$

is the ratio of the rotational diffusion timescale, D_R^{-1}, to that of translational diffusion, a^2/D_T. Other relevant dimensionless parameters are the SPP Péclet number,

$$\mathrm{Pe}_s = \frac{v_s}{aD_R},$$

and the fluid Péclet number,

$$\mathrm{Pe}_f = \frac{u_{\mathrm{in}}}{aD_R} = \frac{u_{\mathrm{in}}}{v_s}\mathrm{Pe}_s.$$

The latter compares the ratio of diffusive time D_R^{-1}, to convection time a/u_{in} or equivalently the ratio of convective length u_{in}/D_R to the characteristic length scale, a.

Equations (7) and (8) show that the system is determined by eight dimensionless parameters: the active particle Péclet number, Pe_s, the fluid Péclet number Pe_f, the active vorticity $\hat{\Omega}_0$ and dimensionless fluid vorticity $\hat{\Omega}_f$, the relative magnitude of the translational diffusion, $\hat{D}_T$, the SPP number density, ρ, the relative size of the channel constriction, L_c/L_y, and the relative channel width with respect to the size of microswimmer, $\hat{L}_y \equiv L_y/a$. The persistent length, $l_p = v_s D_R^{-1}$, is also a relevant length scale in active systems. We will use the dimensionless parameter $\tilde{X} \equiv X/l_p$ whenever a length scale is compared with persistent length.

We will consider achiral SPPs, hence $\hat{\Omega}_0 = 0$, and disregard the interactions among SPPs, hence ρ is not relevant (except for being related to the number of particles simulated, which determine the statistics of the numerical simulations). We will also fix the ratio between the translational and rotational diffusion coefficient. Therefore, we are left with five relevant parameters: two determine the active regime of the SPPs under an incoming fluid flow, and three geometric ones, related to the degree of confinement of the SPPs and the particle asymmetry: Pe_s, Pe_f, L_y/a, L_c/L_y, and λ.

IV. RESULTS

Unless otherwise stated, SPPs are ellipsoids of semiminor axis, $b = 0.5$ μm, and aspect ratio, $\lambda = a/b = 6$, which propel in the channel described in Fig. 1 with constant speed $v_s = 20\ \mu\mathrm{m\,s}^{-1}$ and rotational diffusion $\tau_p = D_R^{-1} = 6.85$ s. which corresponds to a persistent length $l_p = v_s\tau_p =$

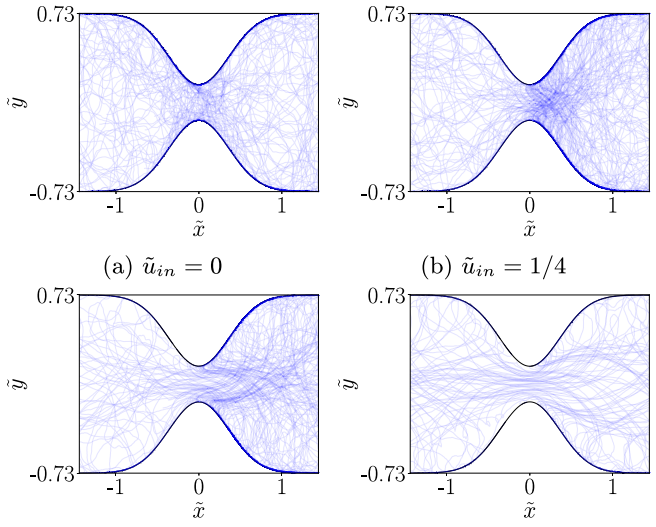

FIG. 2. Trajectories of 50 ellipsoidal particles of aspect ratio $\lambda = 6$ and $\mathrm{Pe}_s = 45.7$ ($v_s = 20\ \mu\mathrm{m\,s}^{-1}$) within a time interval of $t \sim 30\tau_p$. Panels (a)–(d) display the trajectories at four different relative strengths of incoming flow, $\tilde{u}_{\mathrm{in}} = 0, 1/4, 1/2, 1$, corresponding to incoming velocities $u_{\mathrm{in}} = 0, 5, 10, 20\ \mu\mathrm{m\,s}^{-1}$, respectively. In (a) and (d), particles' trajectories distribute uniformly in the right and left sides of the channel, while for intermediate Pe_f (b, c), the trajectories are more concentrated on the right side of the constriction, resulting in asymmetric density profiles.

137 μm, and $\mathrm{Pe}_s = 45.7$. We will also fix the channel width, $a/L_y = 3/200$ and the constriction size, $L_c/L_y = 40/200$. We will hence analyze the relevant regimes varying the relative strength of the incoming flow, $\mathrm{Pe}_f/\mathrm{Pe}_s = u_{\mathrm{in}}/v_s \equiv \tilde{u}_{\mathrm{in}}$, and the SPP asymmetry, λ, and will also consider the impact of the microswimmer persistent length varying l_p/L_y.

A. Trajectories

In order to analyze the qualitative behavior of the system, we first consider SPPs trajectories in the channel as a function of the incoming fluid flow. Figure 2 displays the results of 50 independent (noninteracting) particles for different values of relative incoming flow strengths, $\tilde{u}_{\mathrm{in}} = 0, 1/4, 1/2, 1$, corresponding to incoming fluid velocities $u_{\mathrm{in}} = 0, 5, 10, 20\ \mu\mathrm{m\,s}^{-1}$.

For a static fluid, Fig. 2(a), SPPs are uniformly distributed throughout the channel, while for nonzero incoming fluid velocities [Figs. 2(b) and 2(c)], the right side of the constriction is more crowded. By increasing $\tilde{u}_{\mathrm{in}}$, the asymmetry in the particle population diminishes and finally disappears, as can be seen in Fig. 2(d). This nonmonotonic behavior, which was first observed and reported for dispersion of *E. coli* bacteria through a funnel [17], is a consequence of the interplay between bacteria self-propulsion, fluid flow, and channel confinement. In the following sections we study the time evolution of the SPP probability distribution function, their streamlines, and mean-square displacement to reveal the underlying dynamics of this phenomenon. We will also discuss the controlling parameters which strengthen or weaken the observed symmetry breaking in population density before and after the constriction.

B. Symmetry breaking in probability distribution

In this section we study the time evolution of the probability distribution function (PDF), $p(x)$, starting from a uniform distribution with mean value $p_0 = 1/L_x$ in the channel depicted in Fig. 1.

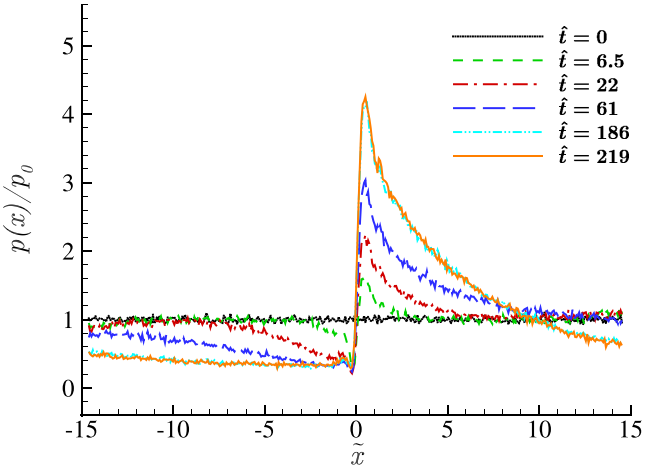

FIG. 3. Time evolution of $p(x)$ for $N = 4 \times 10^4$ ellipsoidal particles of aspect ratio $\lambda = 6$ in the same channel as described in Fig 1, averaged over 10 realizations. Starting from a uniformly distributed state (gray dotted line), the PDF evolves to an asymmetric distribution, for $\hat{t} \gtrsim 200$, with a sharp long-ranged peak just on the right side of the constriction (orange solid line).

The results for a system with $N = 4 \times 10^4$ noninteracting ellipsoidal particles of aspect ratio, $\lambda = 6$, $\mathrm{Pe}_s = 45.7$, and $\tilde{u}_{\mathrm{in}} = 1/4$, are shown in Fig. 3, where the dimensionless PDF, $p(x)/p_0$, is averaged over 10 realizations. The initial, uniform configuration (gray dotted line) evolves to a stationary asymmetric distribution for $t \geqslant 200\tau_p$ (orange solid line). In this stationary state, an abrupt decrease in density before the constriction is followed by a sharp rise just after it, showing that particles are accumulated in the right side of the channel. This is in agreement with the dense trajectory lines observed in Fig. 2(b).

Figure 3 also shows a long-range asymmetric decay of the PDF, which extends through the channel far beyond the constriction, consistent with experimental observations [17]. It is also worth pointing out that $t_s \simeq 200\tau_p$ is a safe enough choice to ensure that the stationary state has been reached and time-averaged quantities are well defined as is observed in other simulations with different parameters (data not shown here).

We may now use the symmetry-breaking parameter,

$$\mathrm{SB} = \frac{N_R - N_L}{N_R + N_L},$$

introduced in [17] to quantify the observed unbalance between the population of particles in the left $[N_L = N \int_{-L_x/2}^{0} p(x)\,dx]$ and right $[N_R = N \int_{0}^{+L_x/2} p(x)\,dx]$ sides of the channel. Figure 4 shows SB as a function of the relative incoming flow strength. Each point is obtained by averaging over 300 snapshots. The previous expression assumes that the system reaches its stationary state at $t = 200\tau_p$. The time interval between two successive snapshots is $\sim 0.07\tau_p$. In agreement with particle trajectories, SB displays a nonmonotonic behavior in response to the increase of $\tilde{u}_{\mathrm{in}}$. We can distinguish three regimes: (1) zero symmetry breaking or homogeneous distribution for $\tilde{u}_{\mathrm{in}} \simeq 0$, (2) nonzero finite symmetry breaking for middle relative flow strength ($0.2 \precsim \tilde{u}_{\mathrm{in}} \precsim 0.6$), and (3) reduction to zero symmetry breaking (or uniform distribution) for large relative flow strengths $\tilde{u}_{\mathrm{in}} \succsim 0.75$. Therefore there exists a critical relative incoming flow strength, $\tilde{u}^*_{\mathrm{in}}$, for which the system experiences the maximum symmetry breaking, SB^* [17].

The SB profile as well as the critical values ($\tilde{u}^*_{\mathrm{in}}$ and SB^*) are influenced by various factors, including particle asymmetry, relative strength of the incoming flow with respect to self-propulsion

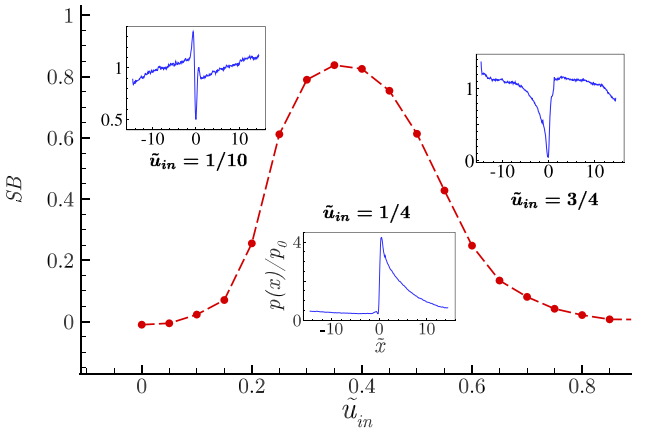

FIG. 4. SB as a function of relative incoming flow strength, $\tilde{u}_{\rm in}$, for SPPs of aspect ratio $\lambda = 6$. Symbols show simulated results; the line is a guide to the eye. Insets show dimensionless PDF $(p(x)/p_0)$ for three special cases, corresponding to $\tilde{u}_{\rm in} = 1/10, 1/4, 3/4$.

speed, and channel confinement. Figure 5 indicates that both SB and $\tilde{u}^*_{\rm in}$ (inset) generically grow with particle elongation, λ.

Figure 6 provides a more comprehensive view of the impact that SPP geometry and incoming flow has on the asymmetric organization of SPPs around the channel constriction. Such a global view is insightful in view of the large disparity of size and shape of artificial and natural SPPs, which range from sphere to needle-like, as well as the different velocities at which they self-propel. Specifically, Fig. 6(a) shows that not only the aspect ratio but also the particle geometry (combination of radii) could influence the value of SB. In the right lower corner of this figure, for instance, we find needle-like particles with large aspect ratio and small SB (almost zero), in contrast to the general trend.

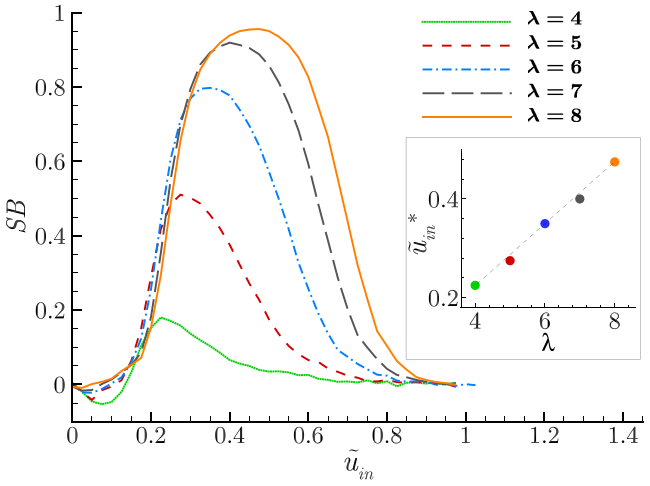

FIG. 5. SB as a function of $\tilde{u}_{\rm in}$ for ellipsoidal particles of various aspect ratios and fixed semiminor axis $b = 0.5$ μm. In the insets, critical relative incoming flow strength, $\tilde{u}^*_{\rm in}$ is plotted as a function of λ, indicating that the peak position increases linearly with particle asymmetry.

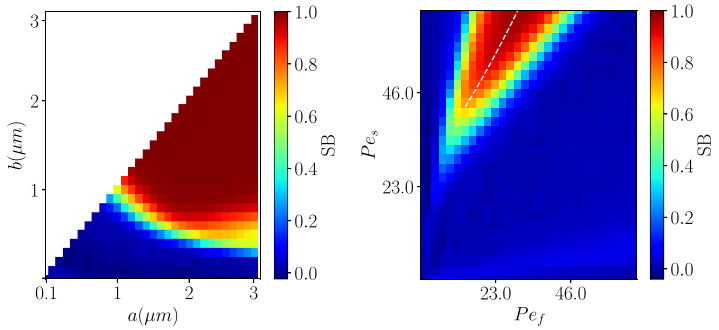

FIG. 6. SB (a) as a function of SPP size and asymmetry for $\tilde{u}_{\text{in}} = 1/4$, $\text{Pe}_s = 45.7$ and (b) as a function of SPPs' and fluid's Péclet numbers for a fixed particle shape, $\lambda = 6$. The rest of the parameters are the same as in Fig. 1.

Figure 6(b) shows the relevant role played by the relative magnitudes of the self-propelling and incoming fluid velocities. For a fixed Pe_s, SB increases from zero to its maximum value and back to zero by increasing Pe_f, in agreement with Fig. 4. For larger propulsion speeds (e.g., $\text{Pe}_s \simeq 70$), symmetry breaking occurs for a wider range of flow velocities, such that the system goes sharply from zero to its maximum value and form a plateau rather than a single maximum point [this is similar to the situation observed for high persistent length (or low $\tilde{L}_y$) in Fig. 7]. The other way around, for a fixed value of Pe_f, SB increases to its maximum value by increasing Pe_s, and returns back to symmetric state when Pe_s becomes large enough.

It is worth noting that the states with equal SB lie on two crossing lines in velocity phase space, which first confirms the existence of a maximum point in SB profile by changing either the fluid or propulsion velocities, and second indicates that there is a unique linear relation between the two velocities for all peak points of SB profile; i.e., all the peak points for various propulsion speeds lie on the same line in velocity phase space, here indicated by a white dashed line: $\text{Pe}_s^* = 1.5\text{Pe}_f^* + 9.7/(aD_R)$.

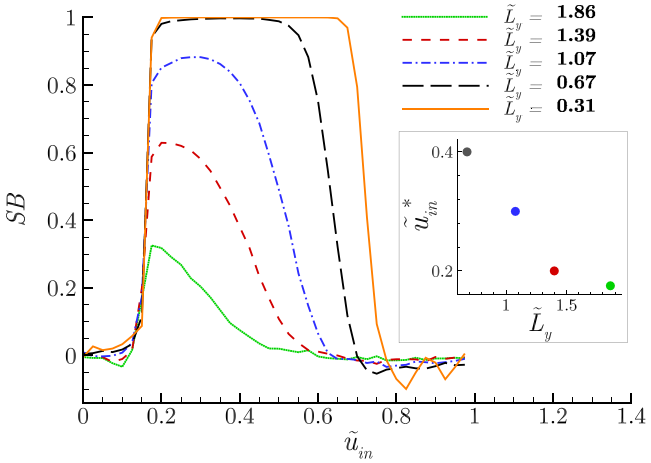

FIG. 7. Symmetry breaking versus relative incoming flow strength for various confinement parameters ($lp/L_y = \tilde{L}_y^{-1}$). Inset shows how the maximum value of the SB profile decreases by decreasing confinement parameter (or increasing $\tilde{L}_y$).

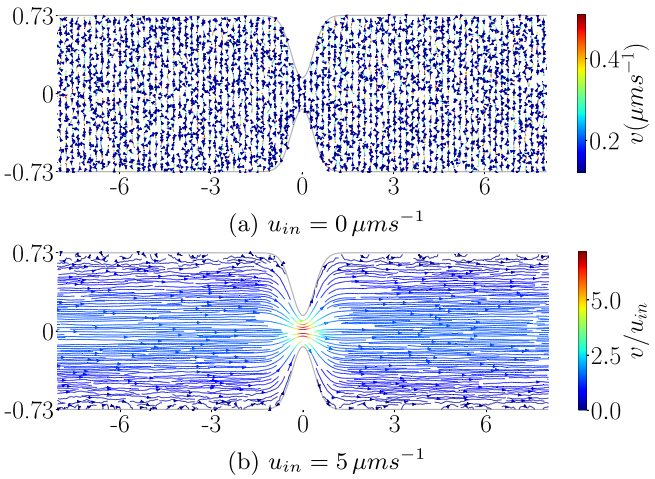

FIG. 8. Streamlines of passive particles ($v_s = 0$) moving in the channel of width $\tilde{L}_y = 1.46$, $\tilde{L}_c = 0.29$, for incoming fluid velocity $u_{\rm in} = 0, 5$ μm s^{-1}. The velocity vector field, $\mathbf{v}(x, y)$, is the local average velocity of particles found in surface element $\delta x \delta y$ around each point, (x, y), in the channel. The color of streamlines changes by the absolute value of average velocity from zero (blue) to its maximum value (red) as shown in the color bar. The triangles on the streamlines show the direction of average velocity field.

The impact of confinement, on the other hand, is characterized by confinement parameter, $l_p/L_y = \tilde{L}_y^{-1}$. The distribution of particles in the channel becomes more asymmetric by decreasing $\tilde{L}_y$, as is indicated in Fig. 7. Note that the single maximum point in the low confinement regime ($\tilde{L}_y > 1$) changes to a plateau in highly confined ($\tilde{L}_y < 1$) cases.

The negative SB region, observed in Figs. 5 and 7 for weak relative fluid strength ($\tilde{u}_{\rm in} \precsim 1/10$), is due to the fact that particles are blocked behind the constriction, then begin to pass it, and aggregate on the right side by increasing the flow velocity.

C. Particle streamlines and upstream flow

In order to understand the types of motion that lead to symmetry breaking, we analyze the SPP streamlines (i.e., local direction of their velocity field). The velocity field, $\mathbf{v}(x, y)$, is obtained by measuring the local average velocity of particles found in surface element $\delta x \delta y$ around the point (x, y), in the channel. In the stream plots, the value and direction of average velocity are shown by colored vectors which, according to the color code given in the side bars, changes from zero velocity (blue) to their maximum magnitude (red). We first analyze the special case of passive particles and then discuss activity-induced effects.

1. Passive particles

Figure 8 displays passive particles ($v_s = 0$) moving in the channel of Fig. 1 with incoming fluid velocity $u_{\rm in} = 0, 5$ μm s^{-1}. As expected, for a fluid at rest [Fig. 8(a)], particles move uniformly in all directions and do not show any preferred direction in their motion. For a net incoming fluid flow [Fig. 8(b)], particles are advected along the flow direction throughout the channel (downstream flow). The local velocity equals the incoming velocity on the left and right walls and is zero on the upper and lower walls as is set by the boundary conditions. Comparing to Fig. 1(b), the local average value of particles' velocity is the same as that of the fluid, indicating that, in agreement with analytical results, the Brownian term in the equations of motion of passive particles is averaged out and the leading term is the fluid velocity. Therefore, passive particles either display Brownian motion, at $u_{\rm in} = 0$, or statistically follow the fluid flow.

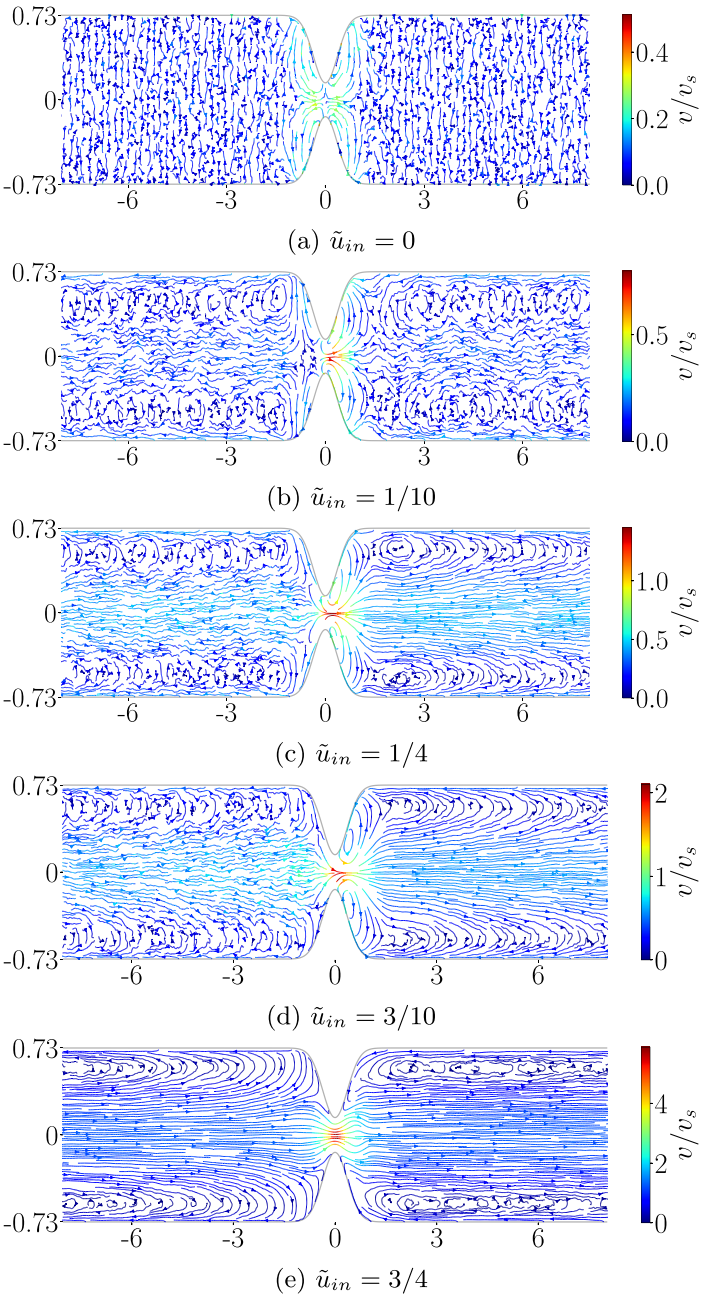

FIG. 9. Streamlines of SPPs of aspect ratio $\lambda = 6$ moving in the same channel as described in Fig. 8 for $\tilde{u}_{\text{in}} = 0, 1/10, 1/4, 3/10, 3/4$. Vertical and horizontal axes are rescaled by l_p.

2. Active particles

Figure 9 displays the streamlines for SPPs of constant Péclet, $\text{Pe}_s = 45.7$, for a fixed channel geometry and increasing incoming fluid flows, $\tilde{u}_{\text{in}} = 0, 1/10, 1/4, 3/10, 3/4$. For a quiescent liquid [Fig. 9(a)] the streamlines do not show a preferred direction and the average velocity essentially

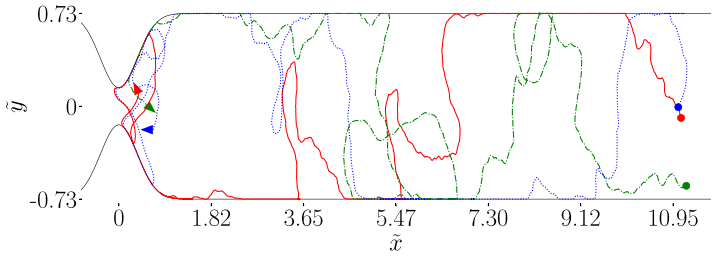

FIG. 10. Typical trajectories of SPPs ($\lambda = 6$) moving upstream in the same channel as described in Fig. 8, for $\mathrm{Pe}_f = 0.3$, corresponding to maximum symmetry breaking. Starting from the right side of the channel (filled circles), particles experience an up-and-down motion between the walls and finally are trapped in a butterfly-like trajectory in front of the constriction. Arrows show the direction of particles' velocity at the ending point of their trajectories.

vanishes, except in the vicinity of the constriction where the velocity is above average and particle self-propulsion forms a symmetric butterfly pattern with its wings extended around the constriction. By comparing with the streamlines of passive particles [Fig. 8(a)], it is apparent that the butterfly pattern is a consequence of the particle self-propulsion in the presence of a constriction.

For nonzero incoming fluid velocities [Figs. 9(b)–9(e)], we observe aligned streamlines in the center of the channel as expected. For intermediate incoming fluid velocities [Fig. 9(b)–9(d)], the butterfly wings observed for a quiescent liquid become progressively more asymmetric, such that for the critical flow velocity where SB is maximized [Fig. 9(d)], the butterfly left wings completely disappear. By further increasing the fluid velocity [Fig. 9(e)] the butterfly pattern is replaced by aligned streamlines indicating that advective motion is dominant.

Comparing the streamline patterns in Fig. 9 with the trajectories in Fig. 2, it can be concluded that the right wings of the butterfly pattern are actually the region where particles are trapped in front of the constriction. This type of attractor is also reported in the motion of sperm cells passing a funnel [25] and magnetotactic bacteria directed upstream through pores subject to external magnetic fields [26]. The extra time spent in the right side of the channel, for net incoming flow, is actually the origin of the observed asymmetric distribution of particles [17]. For low fluid Péclet numbers, $\tilde{u}_{\mathrm{in}} \precsim 1/5$, asymmetric butterfly wings do not develop, while for high Péclet numbers, $\tilde{u}_{\mathrm{in}} \succsim 3/4$, the downstream convective motion is dominant; hence trapping is not possible in these two limiting regimes. The maximum symmetry breaking is therefore observed for intermediate incoming fluid velocities ($1/5 \precsim \tilde{u}_{\mathrm{in}} \precsim 3/5$) where the strength of these opposing effects is balanced.

Upstream flow, i.e., moving in the opposite direction of the flow, is another characteristic feature of SPPs that can reinforce or support symmetry breaking. In contrast to downstream flow, which is the expected motion in the direction of the flow, upstream flow provides the chance for particles that have passed the constriction to move back towards the center of the channel and be trapped in the wings of the butterfly pattern. Figure 10 displays typical particle trajectories starting on the right side of the channel, moving upstream, finally trapped in front of the constriction. Therefore, the trapping probability and thus the value of SB as well as the value of critical velocity are correlated with the ability of particles to perform upstream flow, which itself is affected by the ratio of self-propulsion speed to fluid velocity, the size and shape of particles, or geometry of boundaries.

Particles' streamlines also develop vortices near the upper and lower walls, in which one can easily distinguish the upstream flow in the very first layers close to the walls. The emergence of vortices is due to the interplay of self-propulsion and fluid flow; they disappear for both passive particles moving in a nonzero fluid flow (Fig. 8) and active particles in stationary flow [Fig. 9(a)].

D. Mean-square displacement

The mean-square displacement (MSD) of SPPs provides additional insight into their effective dynamics. The MSD is affected by background fluid flows and/or complexities of the environment,

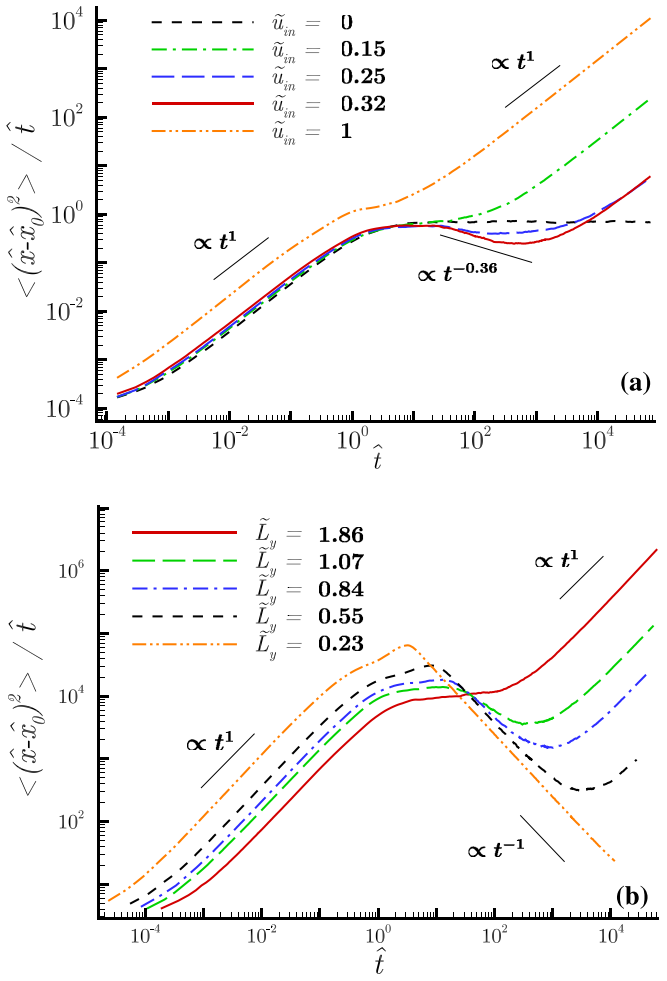

FIG. 11. Mean-square horizontal displacement (MSD) divided by time for (a) ellipsoidal particles of aspect ratio $\lambda = 6$ for different incoming flow $\tilde{u}_{\rm in}$ and (b) spherical particles of different $\tilde{L}_y$ (corresponding to radii $a = 1, 1.2, 1.3, 1.5, 2.0$ μm, respectively) and $\tilde{u}_{\rm in} = 1/4$.

such that multiple transitions from ballistic to diffusive and sub- (or super-) diffusive regimes might be observed.

In the absence of an incoming flow, the MSD of SPPs is characterized by a ballistic and an asymptotic diffusive regimes with a crossover timescale determined by rotational diffusion. Typically, $\tau_D = 1/D_R \simeq 1$–10 s for microorganisms and self-propelling colloids, is much larger than the timescales in which passive colloidal particles of mass m and friction coefficient, γ, enter the diffusive regime, $t_D = m/\gamma \simeq 10^{-9}$ s.

Figure 11 displays the MSD divided by time in dimensionless units for various [Fig. 11(a)] $\tilde{u}_{\rm in}$ and [Fig. 11(b)] $\tilde{L}_y$.

In the absence of an incoming flow [Fig. 11(a)] the MSD crosses over from ballistic to normal diffusive regime at $\tau_D \simeq 10$ s (black dashed line). For nonzero incoming fluid velocities, the diffusive regime lasts for a finite time, and, asymptotically, the MSD shows another crossing to an asymptotic ballistic regime, which is now a consequence of particle advection by the fluid flow. These three regimes are clearly distinguished for low ($\tilde{u}_{\rm in} = 3/20$) and high ($\tilde{u}_{\rm in} = 1$) incoming fluid strengths;

while for intermediate values ($\tilde{u}_{\rm in} = 1/4, 6.5/20$), we observe an extra subdiffusive regime from $\hat{t} \simeq 40$ to 4000, followed by a ballistic regime, which in this case is a very weak advection even compared to the lowest velocity ($\tilde{u}_{\rm in} = 3/20$). This characteristic feature of intermediate velocities confirms the trapping of particles in the channel (i.e., butterfly trajectories), which is the origin of the observed symmetry breaking.

By increasing the persistent length (or decreasing $\tilde{L}_y$), as displayed in Fig. 11(b), the duration of the subdiffusive regime increases, and the final advective motion becomes weaker (note the region with negative slope), in agreement with the increase of symmetry breaking indicated in Fig. 7. The MSD for large persistent lengths (e.g., $\tilde{L}_y = 0.23$) goes asymptotically to a constant value. It eventually becomes ballistic but at much longer times (not shown here), meaning that a high percentage of particles are almost motionless, leading to high symmetry breaking (SB $\simeq 1$) for a wide range of velocities as is also seen in Fig. 7.

V. CONCLUSIONS

We have performed Brownian dynamics simulations to investigate the underlying dynamics that lead to the observed densification of self-propelled particles in confined microchannels with a constriction [17]. The model system considers the general case of self-propelling particles of arbitrary shape and size whose motion are simulated as active Brownian particles. The propelling objects in this model perform an overdamped motion under the action of an internal driving force directed along its orientation, which itself undergoes Brownian fluctuations. In addition, both the translational and rotational degrees of freedom are affected by the nonlinear fluid velocity field in the channel, which is obtained by solving the Stokes equation and assumed to be independent of the propelling objects.

The simulation results indicate that in the stationary state, the particle probability distribution in the channel can be either symmetric or asymmetric with respect to the constriction depending on the value of fluid Péclet number (or the ratio of fluid velocity to self-propulsion speed). The symmetry-breaking parameter (SB), which quantifies the degree of asymmetry, is maximized for intermediate incoming flows, $\mathrm{Pe}_f = 3/10$, while it goes to zero asymptotically for both low and high fluid Péclet numbers, in agreement with experimental evidence [17].

The critical average fluid velocity (with maximum SB) is linearly proportional to the propelling speed of active particles, such that all peak points of SB profile lie on the same line in velocity phase space as shown in Fig. 6. For constant propulsion and fluid velocities, the peak position (Pe_f^*) scales with particle size, and its height (peak value) increases by increasing the size of particles and/or confinement.

A closer analysis of the particle' streamlines has revealed that for intermediate fluid velocities, $1/5 < \mathrm{Pe}_f < 3/5$, particles are trapped in butterfly-like trajectories at the constriction. This pattern traps the self-propelling particles preferentially when they meet the constriction through upstreaming leading to the observed symmetry breaking. The butterfly pattern develops due to the competition between the incoming flow and particle self-propulsion. The attractor, the butterfly pattern, is sustained for intermediate strengths of the incoming flow and depends on, among other parameters, the ratio of propulsion to flow speed and persistent length. The trace of the attractors in MSD plots appears as subdiffusive regimes, whose duration increases for larger particles, in agreement with the larger symmetry breaking observed for larger particles.

The model we have introduced is versatile and can be applied to more complex boundary conditions, different channel geometries, and/or other models of propulsion such as run-and-tumble motion. Building on the reported analogous dynamical behavior of ABP and run and tumble [27], the good agreement with experimental results for *E. coli* suggest that the ABP model for an ellipsoidal particle is able to capture the essential features of the response of *E. coli* in constricted channels. The results reported show that symmetry breaking in confined channels with constriction is a generic property of self-propelling particles, not restricted to special species, or sizes.

ACKNOWLEDGMENTS

This work is supported by Tarbiat Modares University. I.P. acknowledges support from Ministerio de Ciencia, Innovacion y Universidades MCIU/AEI/FEDER for financial support under Grant Agreement No. PID2021-126570NB-100 AEI/FEDER-Eu, from Generalitat de Catalunya under Program Icrea Acadèmia and Project No. 2021SGR-673.

[1] C. Bechinger, R. Di Leonardo, H. Löwen, C. Reichhardt, G. Volpe, and G. Volpe, Active particles in complex and crowded environments, Rev. Mod. Phys. **88**, 045006 (2016).
[2] R. Dey, C. Buness, B. Hokmabad, C. Jin, and C. Maass, Oscillatory rheotaxis of artificial swimmers in microchannels, Nat. Commun. **13**, 2952 (2022).
[3] R. Rusconi, J. Guasto, and R. Stocker, Bacterial transport suppressed by fluid shear, Nat. Phys. **10**, 212 (2014).
[4] H. M. López, J. Gachelin, C. Douarche, H. Auradou, and E. Clément, Turning bacteria suspensions into superfluids, Phys. Rev. Lett. **115**, 028301 (2015).
[5] A. Creppy, E. Clément, C. Douarche, M. V. D'Angelo, and H. Auradou, Effect of motility on the transport of bacteria populations through a porous medium, Phys. Rev. Fluids **4**, 013102 (2019).
[6] G. Jing, A. Zöttl, E. Clément, and A. Lindner, Chirality-induced bacterial rheotaxis in bulk shear flows, Sci. Adv. **6**, eabb2012 (2020).
[7] A. Daddi-Moussa-Ider, M. Lisicki, and A. J. T. M. Mathijssen, Tuning the upstream swimming of microrobots by shape and cargo size, Phys. Rev. Appl. **14**, 024071 (2020).
[8] M. C. Lane, V. Lockatell, G. Monterosso, D. Lamphier, J. Weinert, J. R. Hebel, D. E. Johnson, and H. L. T. Mobley, Role of motility in the colonization of uropathogenic *Escherichia coli* in the urinary tract, Infect. Immun. **73**, 7644 (2005).
[9] N. Figueroa-Morales, A. Riviera, R. Soto, A. Lindner, E. Altshuler, and E. Clément, E. coli supercontaminates narrow ducts fostered by broad run-time distribution, Sci. Adv. **6**, eaay0155 (2020).
[10] A. Zöttl and H. Stark, Nonlinear dynamics of a microswimmer in poiseuille flow, Phys. Rev. Lett. **108**, 218104 (2012).
[11] W. Schmidt, I. S. Aranson, and W. Zimmermann, Suppression of bacterial rheotaxis in wavy channels, Phys. Rev. Res. **4**, 043005 (2022).
[12] R. Alonso-Matilla, B. Chakrabarti, and D. Saintillan, Transport and dispersion of active particles in periodic porous media, Phys. Rev. Fluids **4**, 043101 (2019).
[13] C. Stumpp, J. Lawrence, M. J. Hendry, and M. Maloszewski, Transport and bacterial interactions of three bacterial strains in saturated column experiments, Environ. Sci. Technol. **45**, 2116 (2011).
[14] J. Liu, R. M. Ford, and J. A. Smith, Idling time of motile bacteria contributes to retardation and dispersion in sand porous medium, Environ. Sci. Technol. **45**, 3945 (2011).
[15] M. Dentz, A. Creppy, C. Douarche, E. Clément, and H. Auradou, Dispersion of motile bacteria in a porous medium, J. Fluid Mech. **946**, A33 (2022).
[16] N. F. Morales, E. Altshuler, A. H. García, A. L. Castellanos, and E. Clément, Two-dimensional continuous model for bacterial flows through microfluidic channels, Rev. Cubana Física **30**, 3 (2013).
[17] E. Altshuler, G. Mino, C. Pérez-Penichet, L. del Río, A. Lindner, A. Rousseleta, and E. Clément, Flow-controlled densification and anomalous dispersion of *E. coli* through a constriction, Soft Matter **9**, 1864 (2013).
[18] M. J. Rhodes, *Introduction to Particle Technology* (John Wiley & Sons, West Sussex, England, 2008).
[19] E. M. Purcell, Life at low Reynolds number, Am. J. Phys. **45**, 3 (1977).
[20] B. J. Kirby, *Micro- and Nanoscale Fluid Mechanics: Transport in Microfluidic Devices* (Cambridge University Press, New York, 2010).
[21] F. Perrin, Mouvement brownien d'un ellipsoide—I. Dispersion diélectrique pour des molécules ellipsoidales, J. Phys. Radium **5**, 497 (1934).

[22] G. Jeffery, The motion of ellipsoidal particles immersed in a viscous fluid, Proc. R. Soc. London A **102**, 161 (1922).

[23] G. Volpe, S. Gigan, and G. Volpe, Simulation of the active Brownian motion of a microswimmer, Am. J. Phys. **82**, 659 (2014).

[24] The inlet velocity (or velocity of fluid far from the constriction, i.e., u_{in}) is a better choice as characteristic velocity than $\langle u \rangle$ because the latter depends on the channel width.

[25] M. Zaferani, G. D. Palermo, and A. Abbaspourrad, Strictures of a microchannel impose fierce competition to select for highly motile sperm, Sci. Adv. **5**, eaav2111 (2019).

[26] N. Waisbord, A. Dehkharghani, and J. Guasto, Fluidic bacterial diodes rectify magnetotactic cell motility in porous environments, Nat. Commun. **12**, 5949 (2021).

[27] M. E. Cates and J. Tailleur, When are active Brownian particles and run-and-tumble particles equivalent? Consequences for motility-induced phase separation, Europhys. Lett. **101**, 20010 (2013).